





Formation of Electron Zebra Stripes Observed on 8 September 2017

Megha Pandya¹ , Yusuke Ebihara¹ , Takashi Tanaka² , and Jerry W. Manweiler³ 

¹Research Institute for Sustainable Humanosphere, Kyoto University, Uji, Japan, ²International Research Center for Space and Planetary Environmental Science, Kyoto University, Uji, Japan, ³Fundamental Technologies, LLC, Lawrence, KS, USA

Key Points:

- Zebra stripes commonly appear in energy versus L spectrograms of energetic electrons in the inner magnetosphere
- We performed advection simulation of trapped electrons with electric field obtained by global magnetohydrodynamics (MHD) simulation
- Zebra stripes are consequence of drift echoes triggered by locally enhanced westward electric field along with field-aligned current (FAC)

Correspondence to:

M. Pandya,
pandya.meghamahendra.3j@kyoto-u.ac.jp

Citation:

Pandya, M., Ebihara, Y., Tanaka, T., & Manweiler, J. W. (2023). Formation of electron zebra stripes observed on 8 September 2017. *Journal of Geophysical Research: Space Physics*, 128, e2022JA030950. <https://doi.org/10.1029/2022JA030950>

Received 23 AUG 2022
Accepted 17 MAR 2023

Abstract Zebra stripes are the characteristic structures having repeated hills and valleys in the electron flux intensities observed below $L = 3$. We delineate the fundamental properties and evolution of electron zebra stripes by modeling advection using time-dependent electric fields provided by a global magnetohydrodynamics simulation. At the beginning of the simulation, the electrons were uniformly distributed in longitude. Some electrons moved inward due to enhanced westward electric field transients in the premidnight-postdawn region. The inwardly displaced electrons were confined in a narrow longitudinal range and underwent grad-B and curvature drifts. For any specific fixed position, the electrons periodically passed through the point with an energy dependent period, giving rise to the hills and valleys in the electron differential flux also known as zebra stripes. The valleys of the zebra stripes are composed of the electrons that underwent outward displacement, or no significant radial displacement. On the nightside, the duskside convection cell is skewed toward dawn in the equatorward of the auroral oval, and the westward electric field becomes dominant in the postdawn region, which results in the inward motion of the electrons. The spatial distribution of the westward electric field is consistent with observation. Zebra stripes are a mixture of the electrons that have and have not experienced inward transport due to solar wind-inner magnetosphere coupling by way of the ionosphere.

1. Introduction

Energetic electron flux measurements in the Earth's inner radiation belt and slot region have an unusual maxima and minima at ~ 100 's of keV energies. Since 1960s a multiple local maximum in the electron energy spectra have been studied in the South Atlantic Anomaly region (≤ 800 km altitude) by several researchers (Imhof & Smith, 1965, 1966; Imhof et al., 1973, 1981). (Imhof & Smith, 1965, 1966) first reported a hill in the energy spectra of electrons at 0.75 and 1.3 MeV energies at $L = 1.15$, using measurements from the polar orbiting earth-oriented satellite at 1650 UT on 2 November 1963. Cladis (1966) calculated the energy gain of the electrons due to magnetic field variations for this event and showed that the hill in the energy spectra are the manifestation of electron acceleration by the drift resonance interaction mechanism. Further, Datlowe et al. (1985) studied the energetic electron spectra (6 keV–1 MeV) over several hundred passages of low altitude satellite, namely S81-1, over South Atlantic Anomaly region, from $L = 1.2$ – 2 . They showed that multiple hills persisted for most days irrespective of the geomagnetic activity. According to the DEMETER satellite measurements at $L = 1.1$ – 1.9 , hills in the electron energy spectra have a constant bounce-averaged drift frequencies across the entire inner belt and they are formed as a result of resonant interaction of energetic electrons with ultralow frequency (ULF) waves induced by arrival of dense solar wind plasma during geomagnetically active periods (Sauvaud et al., 2013).

The periodic structures of electrons with regular hills and valleys are thought to be related to azimuthal drift motion of electrons. These structured features resemble zebra-like patterns and hence Ukhorskiy et al. (2014) entitled them as “Zebra stripes.” Combining modeling efforts and measurements made by the Radiation Belt Storm Probes Ion Composition Instrument (RBSPICE) instrument on board Van Allen Probe-A, Ukhorskiy et al. (2014) showed that the quiet time electron zebra stripes pattern in the energy range of 20–250 keV are the result of slow longitudinal drift motion of electrons under the influence of the rotation of the Earth. Liu et al. (2016) made a statistical study of electron zebra stripes at $L < 3$ and showed that the amplitude of the hills is well correlated with the Kp index, indicating some possible role of geomagnetic activity in the generation of zebra stripes. Previous researchers have reported several interesting characteristic features exhibited by hills and valleys in the terrestrial electron zebra stripes. During the intervals of enhanced geomagnetic activity, the electron zebra stripes can appear as a distorted structures when rearranged into L -value versus drift frequency spectrogram (Ukhorskiy et al., 2014). Moreover, the separation between consecutive hills (and valleys) decreases

© 2023 The Authors.

This is an open access article under the terms of the [Creative Commons Attribution-NonCommercial License](https://creativecommons.org/licenses/by-nc/4.0/), which permits use, distribution and reproduction in any medium, provided the original work is properly cited and is not used for commercial purposes.

with time when represented on a drift frequency spectrogram (Lejosne & Roederer, 2016; Liu et al., 2016). Based on the observations, Lejosne and Mozer (2020) studied that the hills in the electron zebra stripes originate from the morning sector (~ 9 magnetic local time [MLT]) while the valleys in the electron zebra stripes originate from the pre-midnight sector (~ 22 MLT).

One common feature of the zebra stripes is a monotonic decrease in energy of each stripe with L . Such dispersed patterns in the energetic electron spectra are believed to be associated with the rapid injection of charged particles from substorms (Lejosne & Mozer, 2020). Several researchers have proposed that zebra stripe is associated with spatial or temporal changes of the electric fields (e.g., Lejosne et al., 2022; Lejosne & Mozer, 2020; Lejosne & Roederer, 2016; Sauvaud et al., 2013; Ukhorskiy et al., 2014). Cladis (1966) was the first to postulate a model to understand the peak formation due to electron acceleration via the drift resonance mechanism. However, Datlowe et al. (1985) suspected this theory as the electron energy gain per drift orbit is very small and hence the time required for the acceleration of electrons becomes too large. The drift resonance mechanism was also found to be inconsistent by Williams & Frank, 1984 for explaining the acceleration of ions. Contrarily, Sauvaud et al. (2013) performed a statistical analysis using DEMETER satellite observations and proposed that zebra stripes during the geomagnetic storms are the consequence of ULF wave interaction with energetic electrons. Nevertheless, this theory stands incompatible with the simultaneous observation of electron and ion zebra stripes. Wang et al. (2017) performed a test particle simulation of the energetic electrons and ions observed by the RBSPICE instrument on board Van Allen Probes during 15–16 February 2014. They employed a uniform, steady dawn-to-dusk convection electric field and the corotation electric field. The study showed that zebra stripes are reasonably reproduced by the convection electric field. For the same event, Lejosne et al. (2022) applied an empirical model for the equatorial vertical drift velocity depending on the AE index. With a formula, the vertical drift velocity is mapped to arbitrary L -value. The timing for the variations of the radial transport (electric field) is found to be valid. Recently, energetic electron flux enhancements distributed across discrete energy levels have been also observed in the inner magnetosphere of the Saturn (Hao et al., 2020; Sun et al., 2021, 2022) and Jupiter (Hao et al., 2020). These features are also named zebra stripes as they resemble the structures observed in the Earth's inner radiation belts. They showed that the electron zebra stripes in the outer planetary magnetosphere indicates the occurrence of global-electric field enhancements. However, a few questions remain regarding the enhanced convection electric field. What is the origin of the electric field involved in the formation of the zebra stripes? If the convection electric field was responsible, why did the convection electric field penetrate deep into the inner magnetosphere with $L < 3$?

The preferential MLT at which the electrons move inward to form the peaks originate is still unresolved. On the basis of observation, specifying MLT is probably not definitive because of inaccuracy in the determination of the history of the drift trajectories. To overcome this challenge and precisely obtain spatio-temporal evolution of the electrons drifting not only in azimuthal direction, but also radial direction, we perform an advection simulation for the electron zebra stripes. We also back-trace the electron trajectory to identify the initial location of the electrons comprising the hills and valleys in the electron differential flux or zebra stripes. Section 2, describes the details of the satellite data and conditions imposed during the simulation. The details of the observation and results of electron zebra stripes from the Van Allen Probes spacecraft and the one inferred from the simulation are presented in Sections 3 and 4. The generation and evolution of electron zebra stripes in the Earth's inner magnetosphere are then discussed and summarized in Sections 5 and 6.

2. Data and Methodology

2.1. Van Allen Probes Data

The Van Allen Probes have an orbital period of ~ 9 hr with an operational perigee at ~ 700 km, an apogee at $\sim 6.2 R_E$ scanning the near-equatorial region at an inclination of $\sim 10^\circ$ (Mauk et al., 2012). In this orbit it is possible to explore the dynamics of energetic electron fluxes and its band-like features namely, electron zebra stripes during the passage of Van Allen Probes through the Earth's inner magnetosphere. In this work we used data from the RBSPICE (Mitchell et al., 2013) aboard NASA's Van Allen Probe-A spacecraft. In this analysis we specifically use the differential electron fluxes binned at 90° pitch angle from the level 3 pitch angle and pressure data from High-Energy resolution, Low Time resolution, Electron Species Rates (ESRHELT) product having 64 logarithmically spaced energy channels covering the energy range of 20–938 keV.

The inner magnetospheric electric fields are recorded by electric field and waves (Wygant et al., 2013) instrument on Van Allen Probes satellite. It comprises of two spin-plane boom pair that stretches 100 m across and one

spin-axis probes stretching 14 m away measuring all the three components of the electric fields. The electric fields are obtained in modified Geocentric Solar Ecliptic (mGSE) coordinate system. Spin-fit electric field y-component is the spin plane electric field, oriented nearly duskward at spin period cadence (~ 11 s) in the mGSE coordinate system (Breneman et al., 2022). The spin fitting procedure involves a least-square fitting for each spin period of the E_y component of the onboard determined spin plane electric field. Here, $\mathbf{V} \times \mathbf{B}$ electric field in the spacecraft frame due to orbital motion of the spacecraft around the Earth is subtracted from the observed electric field.

2.2. Advection Simulation

Assuming that the electrons conserve the first two adiabatic invariants, we solved the following advection equation (Ebihara & Tanaka, 2013),

$$\frac{\partial f}{\partial t} + \frac{1}{RS_b} \frac{\partial}{\partial R} \left(RS_b \left\langle \frac{dR}{dt} \right\rangle f \right) + \frac{1}{S_b} \frac{\partial}{\partial \varphi} \left(S_b \left\langle \frac{d\varphi}{dt} \right\rangle f \right) + \frac{1}{\gamma p} \frac{\partial}{\partial K} \left(\gamma p \left\langle \frac{dK}{dt} \right\rangle f \right) + \frac{1}{x S_b} \frac{\partial}{\partial x} \left(x S_b \frac{dx}{dt} f \right) = \left(-\frac{2f}{\tau_b} \right)_{\text{loss cone}}, \quad (1)$$

where f , R , φ , K , x , p , γ , and τ_b are the phase space density of electrons, the distance from the center of the Earth, the MLT, the kinetic energy, cosine of the equatorial pitch angle, the momentum of a particle, the Lorentz factor, and the bounce period, respectively. The phase space density is as a function of R , φ , K and x . The left-hand side of Equation 1 is identical to that of Equation 1 of Jordanova et al. (2010) when the magnetic field is dipolar. The phase space density of the electrons inside the loss cone decreases with a characteristic timescale of half the bounce period. S_b is given by Roederer (1970).

$$S_b = \int_{s_m'}^{s_m} \left(1 - \frac{B(s)}{B_m} \right)^{-1/2} ds, \quad (2)$$

where s_m and s_m' are mirror points in the Northern and Southern Hemispheres, respectively. B_m is the magnetic field at the mirror point. The bracket pair $\langle \rangle$ denotes the bounce-averaging operator. The bounce-averaged drift velocity is given by (Roederer, 1970)

$$\langle \mathbf{V} \rangle = \frac{p^2}{qm_0 S_b B_0^2} \nabla I \times \mathbf{B}_0 + \frac{\mathbf{E}_0 \times \mathbf{B}_0}{B_0^2}, \quad (3)$$

where q is the charge, and \mathbf{E}_0 and \mathbf{B}_0 are the electric and magnetic fields in the equatorial plane, respectively. I is a function of the equatorial pitch angle, which is given by

$$I = \int_{s_m'}^{s_m} \left(1 - \frac{B(s)}{B_m} \right)^{1/2} ds. \quad (4)$$

The rate of change in the kinetic energy is given by (Northrop, 1963)

$$\left\langle \frac{dK}{dt} \right\rangle = \frac{M}{\gamma} \frac{\partial \langle B \rangle}{\partial t} + q \langle \mathbf{V} \rangle \cdot \mathbf{E}_0, \quad (5)$$

where M is the relativistic magnetic moment, which is given by

$$M = \frac{p^2 (1 - x^2)}{2mB}. \quad (6)$$

The first term on the right-hand side of Equation 5 is omitted since we assume static magnetic field. The rate of change in x (cosine of the equatorial pitch angle) is given by (Ebihara & Tanaka, 2013)

$$\frac{dx}{dt} = \frac{1 - x^2}{x} \left[\frac{K + mc^2}{K^2 + 2mc^2 K} \left\langle \frac{dK}{dt} \right\rangle - \frac{1}{2B_0} \left(\frac{\partial B_0}{\partial t} + \langle \mathbf{V} \rangle \cdot \nabla B_0 \right) \right]. \quad (7)$$

The radial distance in the equatorial plane ranged from 1.2 to 4.0 Earth radii (R_E) with 24 grid points. The MLT is split into 48. The kinetic energy ranged from 10 keV to 2 MeV with 72 grid points. The pitch angle is split into 8. We employed the Lax–Wendroff scheme (Lax & Wendroff, 1960) with the Superbee flux limiter (Roe, 1985) to solve Equation 1. The phase space density is zero at the beginning of the calculation. In Equation 1 we only include the losses of electrons through the loss cone. However, at lower L -values, there is also a presence of plasmaspheric hiss that is responsible for decreasing the intensity of the electrons fluxes but are not capable for depleting the inner belt electrons to form zebra stripe structures within such a short interval of time. Thus, we consider that the contribution of plasmaspheric hiss to the loss of electron fluxes giving rise to the zebra stripes is negligible. The phase space density at the outer boundary at $L = 4.0$ is set to be the relativistic kappa distribution (Xiao et al., 1998) with number density of 1.7 cm^{-3} , characteristic energy of 2.3 keV, and the kappa value of 5.4 (Birn et al., 1997; Christon et al., 1991). The boundary condition does not affect the conclusion of this paper significantly because we focus on the inward transport of the electrons that are initially located at $L = 4.0$.

The magnetic field is assumed to be the dipole field. Assuming that the magnetic field lines are equipotential, we mapped the electric field from the ionosphere to the equatorial plane along the magnetic field lines. No loss processes, other than the loss cone loss, are taken into consideration. For detailed information about the advection simulation, readers may refer Ebihara and Tanaka (2013). We began the advection simulation at 1800 UT on 7 September 2017, and demonstrate the directional differential flux j given by

$$j = p^2 f. \quad (8)$$

2.3. Global MHD Simulation

To obtain the electric field, we used the global MHD simulation developed by Tanaka (2015). The following is a brief summary of the MHD simulation. The inner boundary of the magnetospheric domain is located on the sphere at $2.6 R_E$. First, we divide the sphere into 12 pentagons. Each pentagon is further divided into 5 triangles. In total, 60 triangles are present in the sphere. We call this Level 1. Each triangle is further divided into 4. Then, we have 240 triangles. We call this Level 2. By repeating the same procedure, we used the Level 6 grid system in which 61,440 triangles are embedded in the sphere. Secondly, 320 triangular prisms are stacked from the inner sphere to $200 R_E$ at midnight and $600 R_E$ at noon.

We determined the ionospheric conductivity by using variables at the inner boundary of the magnetospheric domain. For the contribution from the solar extreme ultraviolet, we determined the ionospheric conductivity depending on the solar zenith angle. For the contribution from discrete auroras, we increased the conductivity in the region where the upward FACs flow. For the contribution from the diffuse auroras, we increased the conductivity in the region where the plasma pressure and the temperature are high. For given the ionospheric conductivity and the FACs, we solved the following partial differential equation to obtain the electric potential at all the magnetic latitudes (Tanaka, 1994).

$$\nabla \cdot (\Sigma \nabla \Phi_i) = -j_{\parallel}, \quad (9)$$

where Σ , Φ_i and j_{\parallel} are the height-integrated ionospheric conductivity tensor, the ionospheric electric potential, and FACs, respectively. The height-integrated conductivity tensor Σ is provided by Ebihara et al. (2014). Although the FAC is provided at magnetic latitudes larger than 51.7° , we can obtain the electric potential from pole to pole. The ionospheric electric field is mapped to the inner boundary of the magnetospheric domain, which is used to determine the inner boundary condition of the plasma flow. For more detailed information about the calculation of the ionospheric conductivity, referers may refer (Ebihara et al., 2014). The solar wind parameters (the solar wind velocity, the solar wind density, interplanetary magnetic field [IMF] By and IMF Bz) provided by the 1-min resolution of the OMNI database (King & Papitashvili, 2005, 2020) were used to the global MHD simulation as the boundary condition.

2.4. Test Particle Simulation

In order to obtain a detailed understanding of motion of the electrons, we also utilize test particle simulations by solving the bounce-averaged trajectories of electrons through solving Equations 3, 5, and 7 simultaneously.

The magnetic and electric fields used for the test particle simulation are the same as those used by the advection simulation.

3. Observation

The solar wind and geomagnetic conditions during 7–8 September 2017 are shown in Figure 1. One-minute resolution data from OMNI dataset is shown in panels (a) solar wind velocity (V_{sw}), (b) solar wind number density (1/cc), (c) Interplanetary magnetic field y-component (IMF B_y), (d) Interplanetary magnetic field z-component (IMF B_z), and (e) symmetric component of geomagnetic disturbance fields (Sym-H) for 7–8 September 2017. At ~ 2300 UT on 7 September 2017, the solar wind velocity jumped from ~ 470 to 707 km/s along with the southward turning of the IMF B_z with the minimum peak value of -31.17 nT. A geomagnetic storm initiated at the same time during which the Sym-H index shows a rapid increase (from -13 to 9 nT), followed by the decrease to a minimum Sym-H value of -143 nT within 2 hr.

Figures 2a–2e presents the energy versus L -value spectrogram of directional differential electron fluxes at 90° pitch angle measured by the RBSPICE instrument during inbound and outbound passage of Van Allen Probe-A. Panel (f) shows the spin-fit y-component of the electric field (E_y) in mGSE coordinate system for the period of between 1200 UT on 7 September to 2359 UT on 8 September 2017. The duration over which the electron zebra stripes were recorded by the Van Allen Probes-A in panel (a–e) are indicated by the yellow shaded portion in panel (f). During the interval between 1554 UT and 1712 UT on 7 September 2017 (panel-a), distinct well organized patterns appear in the spectrum, which is known as zebra stripes (Ukhorskiy et al., 2014). The zebra stripes almost disappeared during the next orbital pass (between 2351 UT on 7 September and 0052 UT on 8 September [panel-b]) during which a sharp jump in the E_y component is observed (panel f) that is associated with the sudden changes in the V_{sw} and IMF B_z (Figure 1). Panel-c shows distorted electron zebra stripes below $L = 3$, which provides an indication of the historical distortion of the electron drift shells. Apart from the distorted zebra stripes pattern in panel-c, it is interesting to observe a sudden electron flux enhancement with <400 keV energies at $L > 2.8$. This may be referred to as sudden particle enhancements at low L shells (SPELLS), in which during geomagnetically active conditions the electrons with ~ 50 keV to ~ 1 MeV energies fill the slot region and penetrates to the Earth's inner radiation belt (Turner et al., 2017). We will mention the relationship between SPELLS and the zebra stripes later. A new set of zebra stripes were rebuilt during the recovery phase of the magnetic storm, which were clearly seen at 0951 UT to 1105 UT on 8 September 2017 onward (panel d–e). The intervals of the stripes in energy are broader than observed before the magnetic storm.

We started the global MHD simulation at 1300 UT on 7 September 2017, and started the advection simulation at 1600 UT on 7 September 2017. The starting time is well before the sudden increase in the solar wind velocity and long-lasting large-amplitude southward component of IMF. The timing is also well before the disappearance of the zebra stripes that occurred between 2032 UT on 7 September and 0052 UT on 8 September 2017. The solar wind velocity suddenly increased at ~ 2345 UT on 6 September 2017 due to the arrival of a coronal mass ejection (CME). We suppose that the contribution from the passage of this CME is minor, and the start time of the two simulations (1300 UT and 1600 UT on 7 September 2017) is reasonable because of the following reasons. First, the southward component of IMF was small associated with the CME that arrived at the Earth ~ 2345 UT on 6 September 2017. Dst does not show a clear negative excursion. This implies that the FACs and the magnetospheric convection were weak, and the impact on the electron distribution was probably minor. The shock could result in the enhancements of the FACs and the magnetospheric convection, but these enhancements associated with a shock usually lasts for a few tens of minutes. The duration of this shock is probably too short to change the keV-range electrons. Secondly, as shown below, the electrons comprising the zebra could depart the outer region around 00–03 UT on 7 September 2017.

4. Simulation Result

4.1. Advection Simulation

Figure 3 shows the calculated spectrograms of the differential electron energy flux at midnight at 0000, 0300, 0600, and 1200 UT on 8 September 2017. Here, the equatorial pitch angle of the electrons is 67.7° . At 0000 UT on 8 September, electrons with energies between ~ 20 keV and ~ 2 MeV are shown barely penetrating into the inner region. The flux monotonically decreases with energy, and no zebra strips present. As mentioned below, this

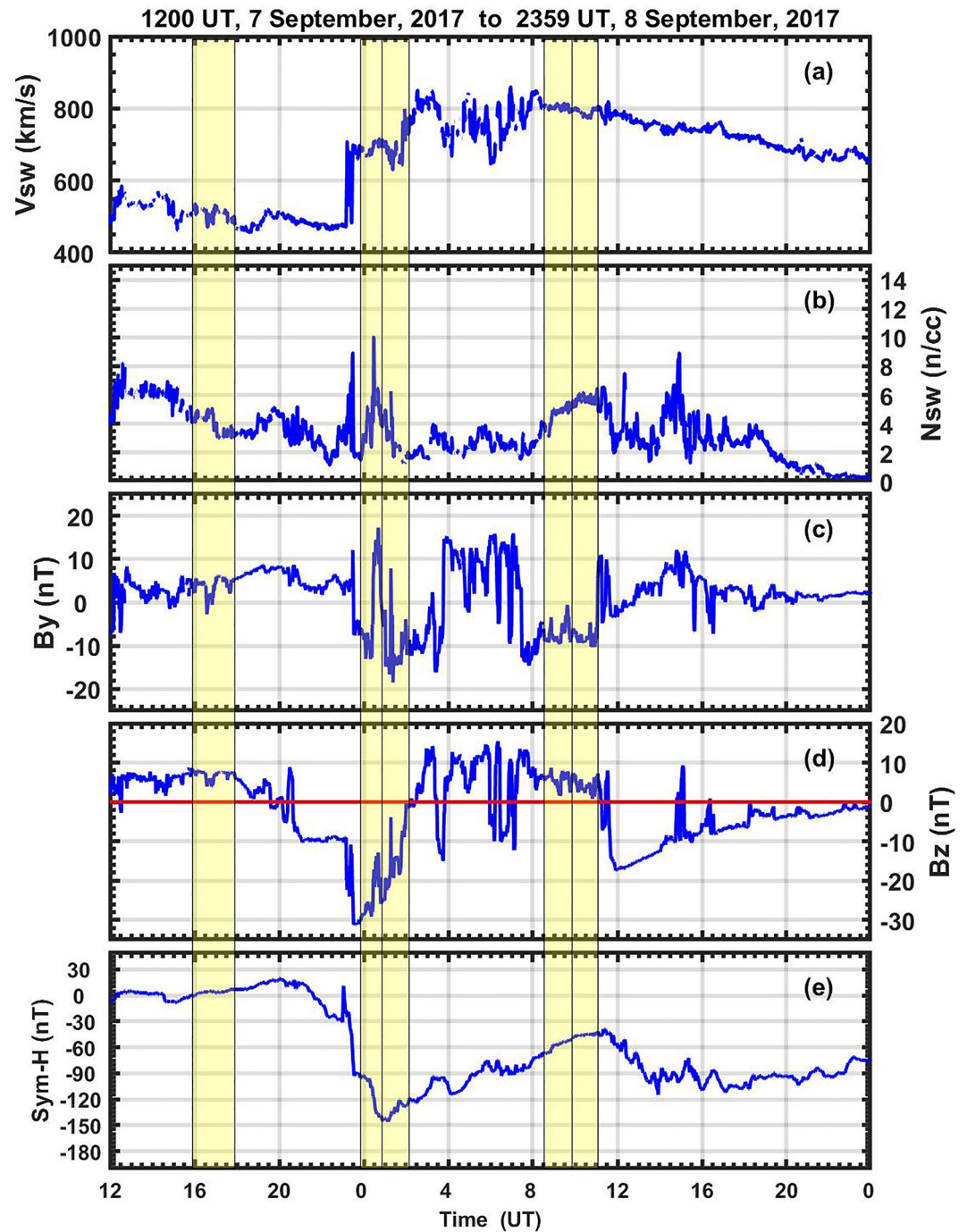


Figure 1. (a) Solar wind velocity, (b) solar wind number density, (c) interplanetary magnetic field (IMF) y-component (IMF By), (d) IMF (Bz), and (e) Sym-H index for the period of between 1200 UT on 7 September to 2359 UT on 8 September 2017.

electron population is freshly transported from the outer region, and is similar to SPELLS (Turner et al., 2017). As the magnetic storm proceeds, electrons with energies below ~ 50 keV penetrate to $L \sim 2.5$ and stripes are becoming distinct at energies larger than 100 keV. At 0600 and 1200 UT, distinct almost evenly spaced hills and valleys in the energy spectrum develop, resembling the zebra stripe pattern in the differential flux. To analyze the generation of hills and valleys in the electron flux intensities, we focus on the electron fluxes at 1200 UT on 8 September, and arbitrarily selected the electron flux at $L = 3$ at midnight indicated by the black vertical line.

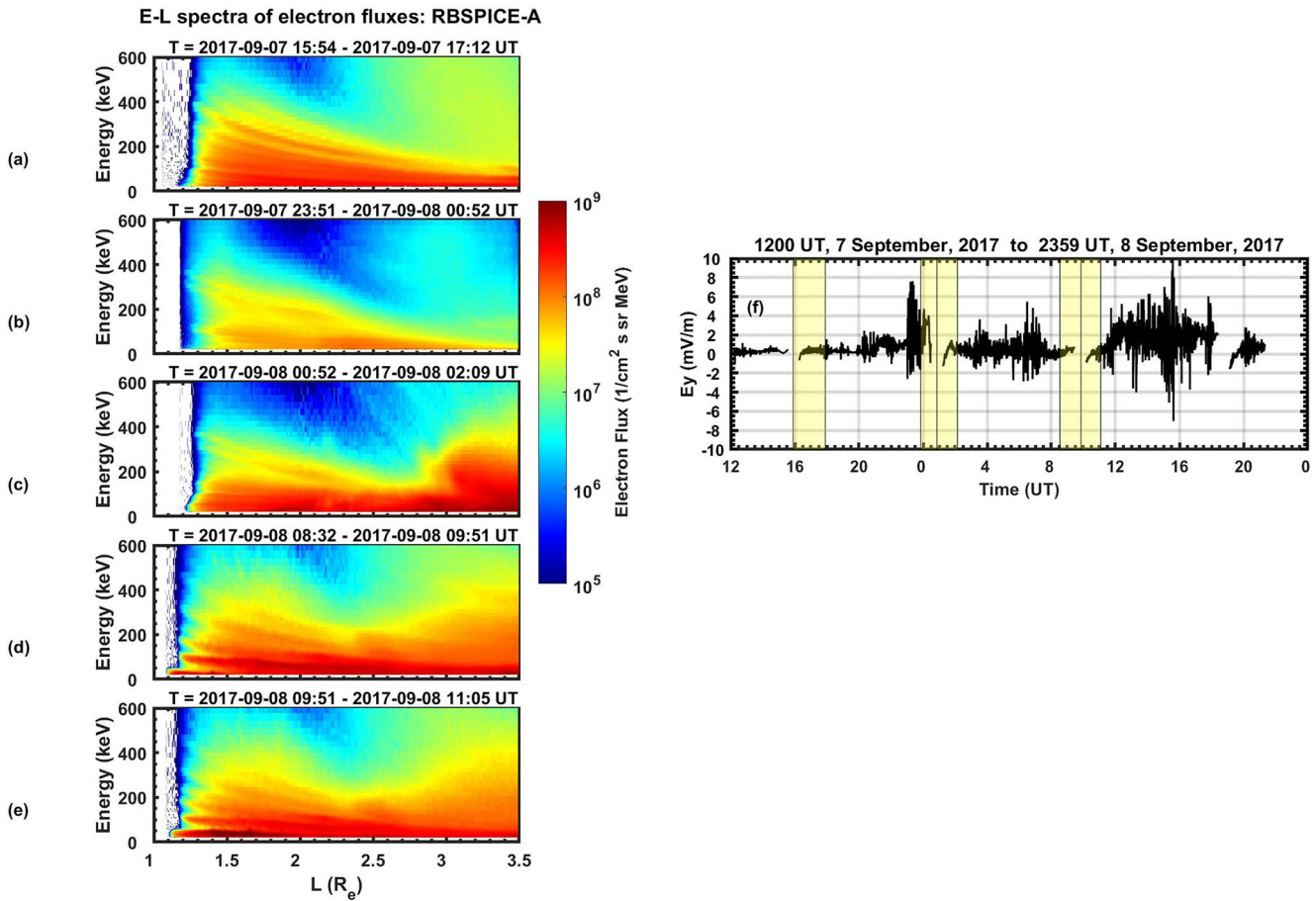


Figure 2. Energy versus L-value spectrograms of 90° pitch angle electron fluxes measured by Radiation Belt Storm Probes Ion Composition Instrument onboard Van Allen Probe-A on 7–8 September 2017 panels (a–e). Distinct electron zebra stripes were observed in the energy range of 20–500 keV. The consecutive inbound and outbound passes of the spacecraft are shown. On each pass, the spacecraft crossed $1 < L < 2.5$ from midnight to the dawn sector and from dusk to midnight sector. Panel (f) shows the spin-fit electric field (E_y component) recorded by the Van Allen Probes-A for the period of between 1200 UT on 7 September to 2359 UT on 8 September 2017. The periods of the observation shown in Panels a–e are indicated by shaded yellow portions in Figures 1 and 2f.

Figure 4 shows a spectrum of the electron differential flux at $L = 3$ and midnight at 1200 UT on 8 September. The maximum and minimum intensities of the electron fluxes at $L = 3$ are clearly observed. The peak flux values are indicated by the pink circles and the cyan boxes with the corresponding peak energies. The meaning of the cyan boxes will be described later. The green circles are placed at local minimum in the electron differential flux.

Figure 5 shows the L-MLT distribution of the electron flux intensities in the equatorial plane at (a) 21.09 keV, (b) 35.55 keV, (c) 55.64 keV, (d) 87.06 keV, (e) 197.85 keV (f) 26.38 201 keV (g) 47.92 keV (h) 69.60 keV, (i) 117.35 keV, and (j) 170.42 keV at 1200 UT on 8 September 2017. The top panels (a–e) show electron fluxes that exhibits hills at $L = 3$ at midnight, while the lower panels (f–j) show those exhibiting valleys at $L = 3$ at midnight. The arrows indicate the direction of the electric field (including the corotation electric field) while the length of the vector gives the magnitude. The electron fluxes have an asymmetric distribution in MLT. At a given L-value and MLT the flux increases and decreases in accordance with the energy dependent grad-B and curvature drift of the electrons, giving rise to the peak and valleys at a fixed position.

4.2. Test Particle Simulation

Figure 6 summarizes the L-value, the azimuthal component of the electric field (E_ϕ), MLT and the kinetic energy along the trajectories of the electrons that contribute to the hills of the fluxes indicated by the pink circles in Figure 4. The trajectories are traced backward in time from the point at $L = 3$ and midnight at 1200 UT on 8 September 2017. The electron energies at the beginning of the backward tracing are 21.09 keV (black), 35.55 keV

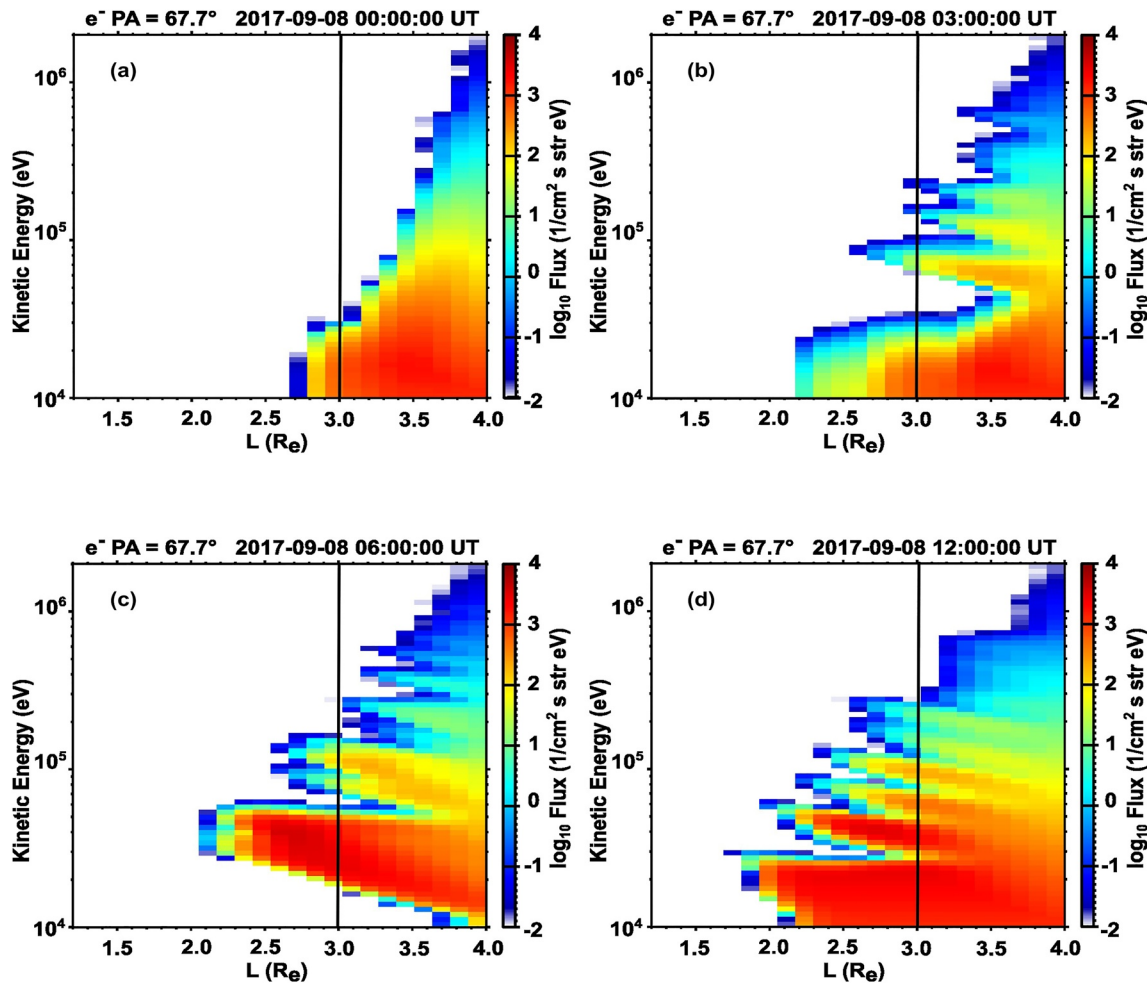


Figure 3. Energy- L^* spectrogram of electron fluxes obtained from global magnetohydrodynamics simulation at (a) 0000 UT, (b) 0300 UT, (c) 0600 UT, and (d) 1200 UT on 8 September 2017. The equatorial pitch angle of the electrons is 67.7° . Black vertical line indicates $L = 3$.

(pink), 55.64 keV (blue), 87.06 keV (cyan), and 197.85 keV (magenta). The equatorial pitch angle was set to be 67.7° . The circles in panel (a) corresponds to the times at which the electrons contributing to the hills are injected into the system at $L = 4$. Hereinafter, it is referred to as start time (T_{start}).

Figure 6a shows the L -values of the electrons. After departing $L = 4$, the electrons moved to lower L -values for 60–108 min. The inward transport is associated with the sustained enhancements of the westward electric field (negative E_p) as shown in Figure 6b. The westward electric field gives rise to the inward transport of the electrons due to the $E \times B$ drift. The inward transport took place ~ 22 –08 MLT that is, premidnight-dawn region as shown in Figure 6c. During the inward transport the electrons gain energy as shown in Figure 6d. The characteristic features of electrons that contribute to the hills of zebra are summarized in Table 1.

Figure 7 is the same as Figure 6 except for the electrons comprising of the valleys indicated by the green circles in Figure 4. Again, the trajectories of electrons are traced backward in time starting at 1200 UT, $L = 3$ and midnight, with the initial electron pitch angle 67.7° . The initial energies of the valley electrons are 26.38 keV (black), 47.92 keV (pink), 69.60 keV (blue), 117.35 keV (cyan), and 170.42 keV (magenta). Contrary to the electrons composing the hills, as shown in Figure 7a, the electrons composing the valleys are not coming from the outer boundary of $L = 4$. The valley electrons come from $L \sim 2.4$ – 3.2 . In the beginning of the advection simulation the phase space density of the electrons is set to be zero everywhere. Hence according to Liouville's theorem the resultant flux should be zero. During the formation of the valleys the westward component of the electric field is not enhanced for prolong for a long period of time, whereas the eastward component is significantly enhanced. The phase space density of the electrons comprising the valleys is not always zero because of numerical diffusion that occurs when we solve Equation 1.

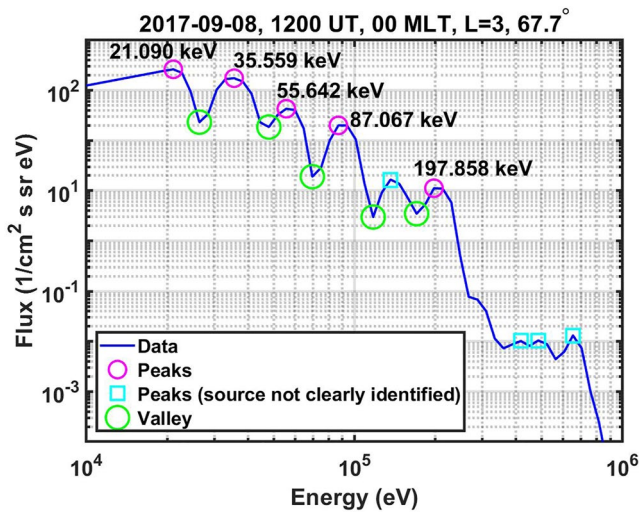


Figure 4. Differential fluxes of electrons at $L = 3$, midnight, at 1200 UT on 8 September 2017, which are taken along the black vertical line in Figure 3. Pink and cyan circles indicate the peak fluxes at the given energies. The origin of the peak fluxes indicated by the cyan boxes is uncertain probably due to numerical diffusion. The green circles indicate the valleys of the fluxes.

Figure 8 shows the distributions of the FAC (FAC), ionospheric Hall conductivity, the electric potential, and eastward component of the ionospheric electric field in the ionosphere in the Northern Hemisphere. As shown in Figure 8a, two pairs of the large-scale FACs are clearly demonstrated. The poleward pair corresponds to the Region 1 FACs, and the equatorward one corresponds to the Region 2 FACs. At 2300 UT on 7 September 2017, the magnitude of the Region 1 FACs is fairly weak. The magnitude of the Region 1 FACs increased around 0000 UT on 8 September 2017, and decreased by 0300 UT. Figure 8b shows the height-integrated ionospheric Hall conductivity, which can be, in part, regarded as aurora. At a glance, the ionospheric conductivity is distributed as if it surrounds the magnetic north pole. This may correspond to the auroral oval. Hereinafter, we call it an auroral oval. At 0000 UT on 8 September, the equatorward boundary of the auroral oval moves equatorward. In Figure 8c, the two-cell ionospheric electric potential pattern is shown. In general, the potential is positive on the dawnside, and negative on the duskside. The ionospheric Hall current flows along the equipotential line. On the nightside, the Hall current flows, in general, from low to high latitudes. The Hall current significantly increases when it flows from the low latitudes into the auroral oval because of the large positive gradient of the conductivity along the Hall current. The discontinuity of the Hall current gives rise to accumulation of negative space charge at the equatorward edge of the auroral oval, which can be regarded as polarization. The negative space charge concentrated at the equatorward edge of the auroral oval leads to an

associated the elongation of the dusk cell (negative potential) to the dawnside. The elongation of the dusk cell results in the extension of the region where the westward electric field extends to the dawnside as shown in Figure 8d. Figure 8d shows the azimuthal component of the ionospheric electric field (positive eastward). The westward electric field appears to dominate over the wide region from ~ 2100 MLT to 0900 MLT at low latitudes. At 0100 UT, the Region 1 FACs further increased, resulting in the enhancements of the ionospheric potential, and the westward electric field. At 0200 UT, the Region 1 FACs are confined to the higher latitudes. The ionospheric conductivity also contracts, and the electrical potential and the electric field decreases. At 0300 UT, the FACs, the ionospheric conductivity, the electrical potential and the electric field diminishes to negligible values.

Figure 9 shows the azimuthal component of the ionospheric electric field at 50 MLAT as a function of MLT and time. The westward electric field (negative value) is enhanced from the premidnight to the dawn-noon sector

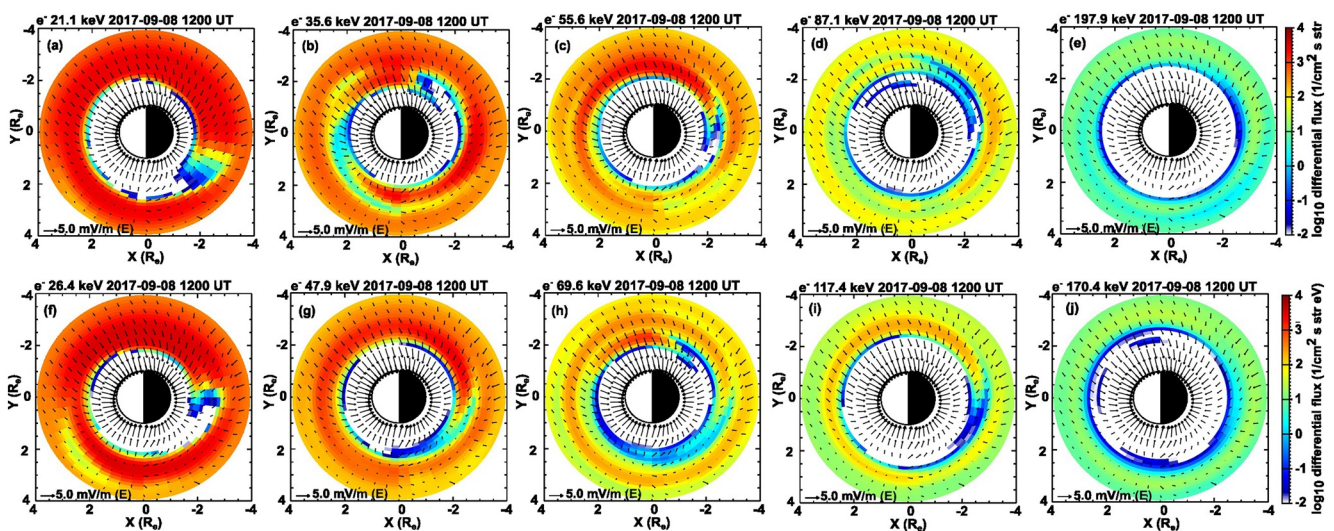


Figure 5. Snapshots of fluxes of (a) 21.09 keV, (b) 35.55 keV, (c) 55.64 keV, (d) 87.06 keV, (e) 197.85 keV (f) 26.38 keV (g) 47.92 keV (h) 69.60 keV, (i) 117.35 keV, (j) 170.42 keV electrons in the equatorial plane at 1200 UT on 8 September 2017. The equatorial pitch angle is 67.7° . The arrows indicate the electric field.

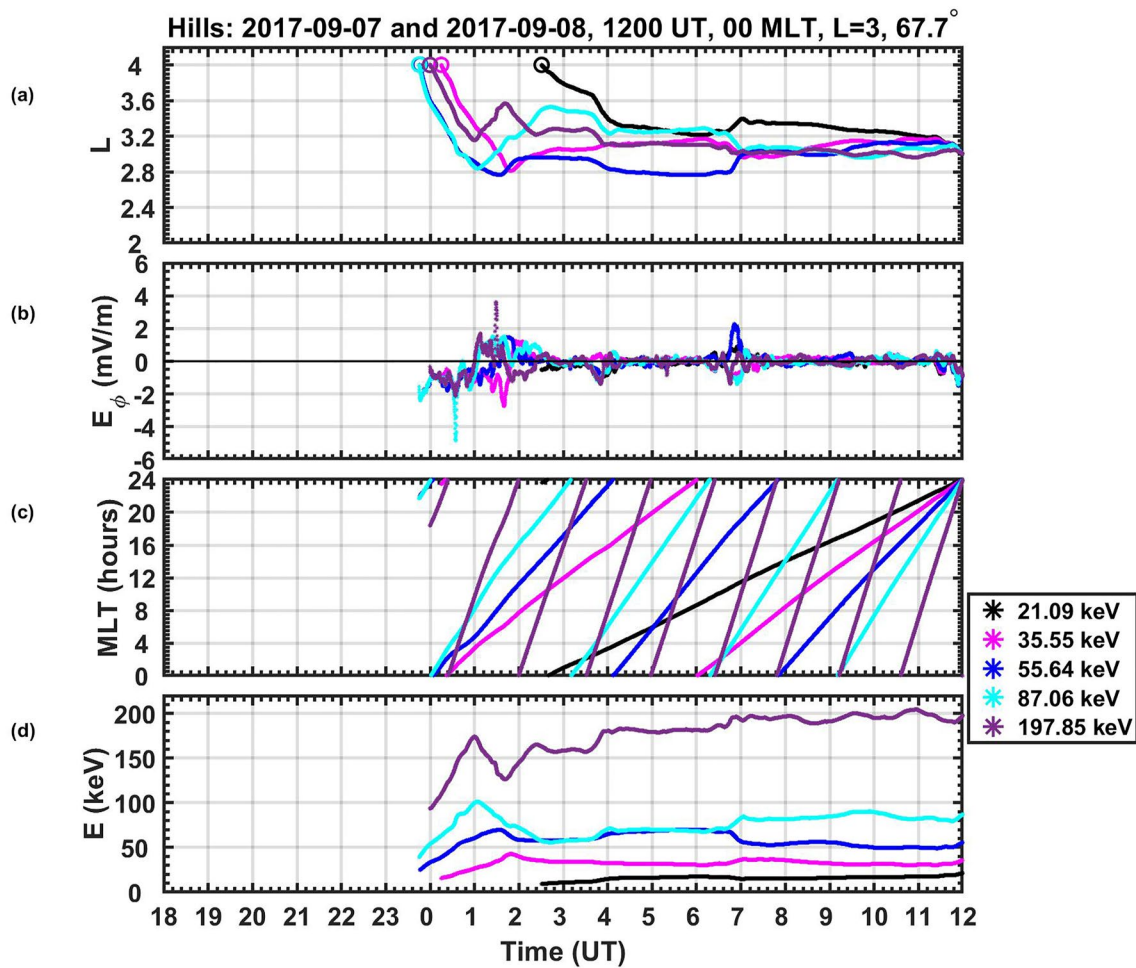


Figure 6. Simulated trajectories of five electrons constituting the hills in the electron fluxes under the real solar wind conditions. Initial energies of the electrons are 21.09 keV (black) 35.55 keV, (pink) 55.64 keV, (blue) 87.06 keV, (cyan) 197.85 keV (magenta) starting at 0000 magnetic local time (MLT), $3 R_E$ and 1200 UT on 8 September 2017. The initial pitch angle is set at 67.7° . The L-value (a), azimuthal component of the electric field, E_ϕ , (b), MLT (c), and energy, E, (d) are shown as a function of time.

between ~ 2330 UT on 7 September and 0130 UT on 8 September. During this interval, the significant earthward transport of the electrons took place as summarized in Table 1. The eastward electric field (positive value) is enhanced in two regions, the postdawn-postnoon region, and the postdusk region. The discontinuities of the electric field found around dusk and dawn are associated with the terminator (~ 06 MLT and ~ 18 MLT) at which the gradient of the ionospheric conductivity is large. These localized enhancements have already been presented by Senior and Blanc (1984), Tsunomura (1999), and Wolf (1970). The modulation of the electric field is caused by the polarization associated with the gradient of the ionospheric conductivity (Wolf, 1970). The distribution

Table 1
The Characteristics of 21.09, 35.55, 55.64, 87.06, and 197.85 keV Electrons Giving Rise to the Hills Indicated by the Pink Circles in Figure 4

	21.09 keV	35.55 keV	55.64 keV	87.06 keV	197.85 keV
UT at which electron departs $L = 4$ (T_{start})	0230 UT	0015 UT	2346 UT	2345 UT	2359 UT
	8 September 2017	7 September 2017	7 September 2017	8 September 2017	8 September 2017
Duration of initial inward transport (min)	89	94	108	79	60
Magnetic local time range of initial inward transport	2335–0317	2327–0648	2201–0832	2141–0851	1825–0939
Averaged radial speed of initial inward transport (R_E/s)	-6.67×10^{-3}	-12.7×10^{-3}	-11.50×10^{-3}	-14.67×10^{-3}	-14.00×10^{-3}
Averaged E_ϕ in initial inward transport (mV/m)	-0.14	-0.011	-0.11	-0.11	-0.11

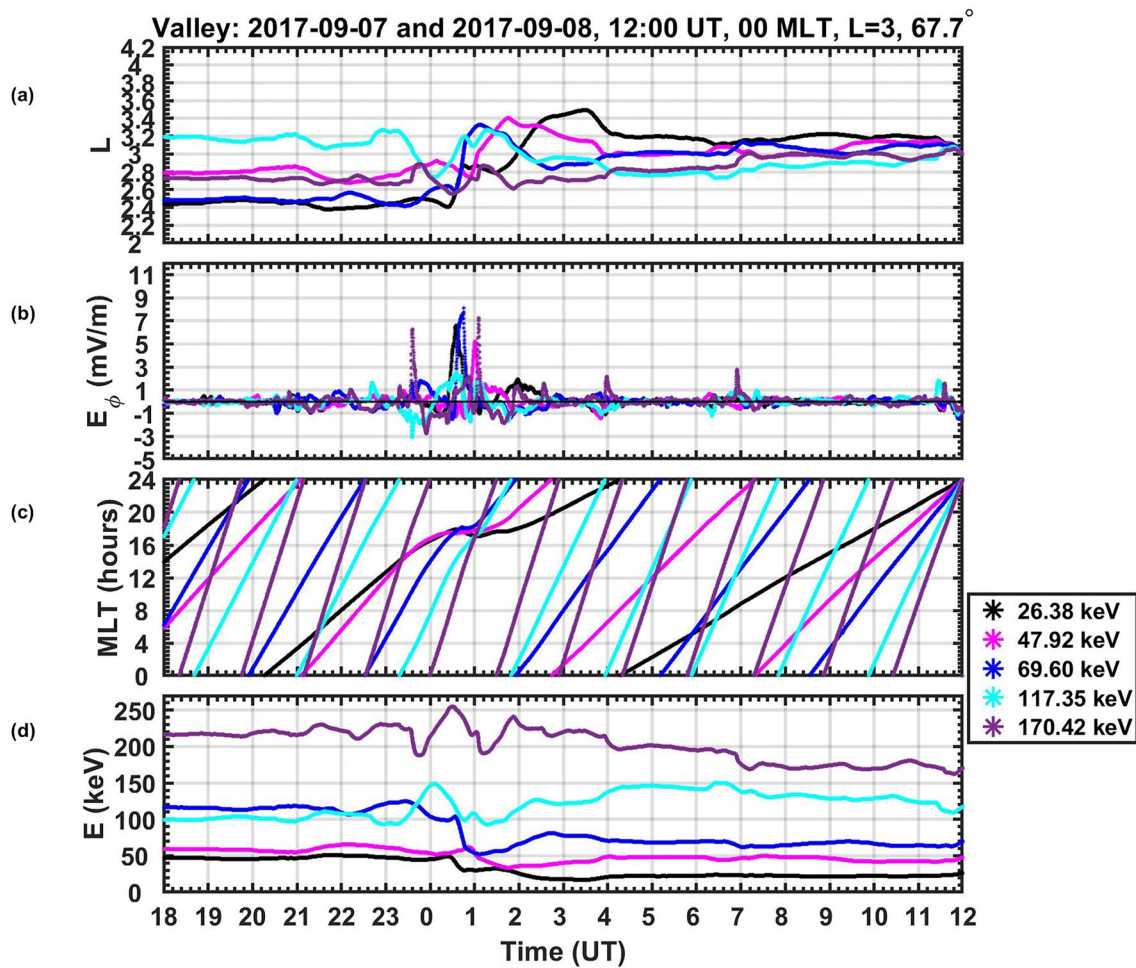


Figure 7. Representation of panels (a–d) are same as Figure 6 except for five electrons constituting the valleys in the electron fluxes. Initial energies of the electrons are 26.38 keV (black), 47.92 keV (pink), 69.60 keV (blue), 117.35 keV (cyan), 170.42 keV (magenta) starting at 0000 magnetic local time, 3 R_E and 1200 UT on 8 September 2017.

of the azimuthal component of the electric field are, in general, consistent with the observation made during the intervals associated with zebra stripes as shown in Figure 9 of Lejosne and Mozer (2020).

5. Discussion

The direct cause of the zebra stripes is thought to be the enhancement of the convection electric field. When the westward electric field is enhanced, electrons move earthward by $E \times B$ drift as shown in Figure 6a, which gives rise to flux enhancements similar to SPELLS (Turner et al., 2017). When the electric field is weakened, the electrons drift eastward by the grad-B and curvature drifts, giving rise to zebra stripes. In that sense, SPELLS could be a manifestation of freshly transported electrons, and a source population of the zebra stripes.

In the simulation, the origin of the convection electric field is ionospheric space charge deposited by the Region 1 FACs. Cladis (1966) indicated that geomagnetic field fluctuations at lower altitudes are the results of local ionospheric currents. The geomagnetic variations are shown to be coherent from high to low latitudes in response to variations of IMF due to simultaneous development of the DP2 current (Nishida, 1968). The DP2 current, which is the two-cell Hall ionospheric current, is suggested to be driven by the Region 1 FACs (Kikuchi et al., 1996). In response to the increased interaction between the fast solar wind plasma and the magnetic field of the Earth, the low-latitude boundary layer and the high-latitude boundary layer favor the generation of the Region 1 FACs that connects the Earth's magnetosphere and the ionosphere (Bythrow et al., 1981; Cowley, 1982; Eastman et al., 1976; Echim et al., 2008; Iijima, 2000; Johnson & Wing, 2015; De Keyser & Echim, 2013;

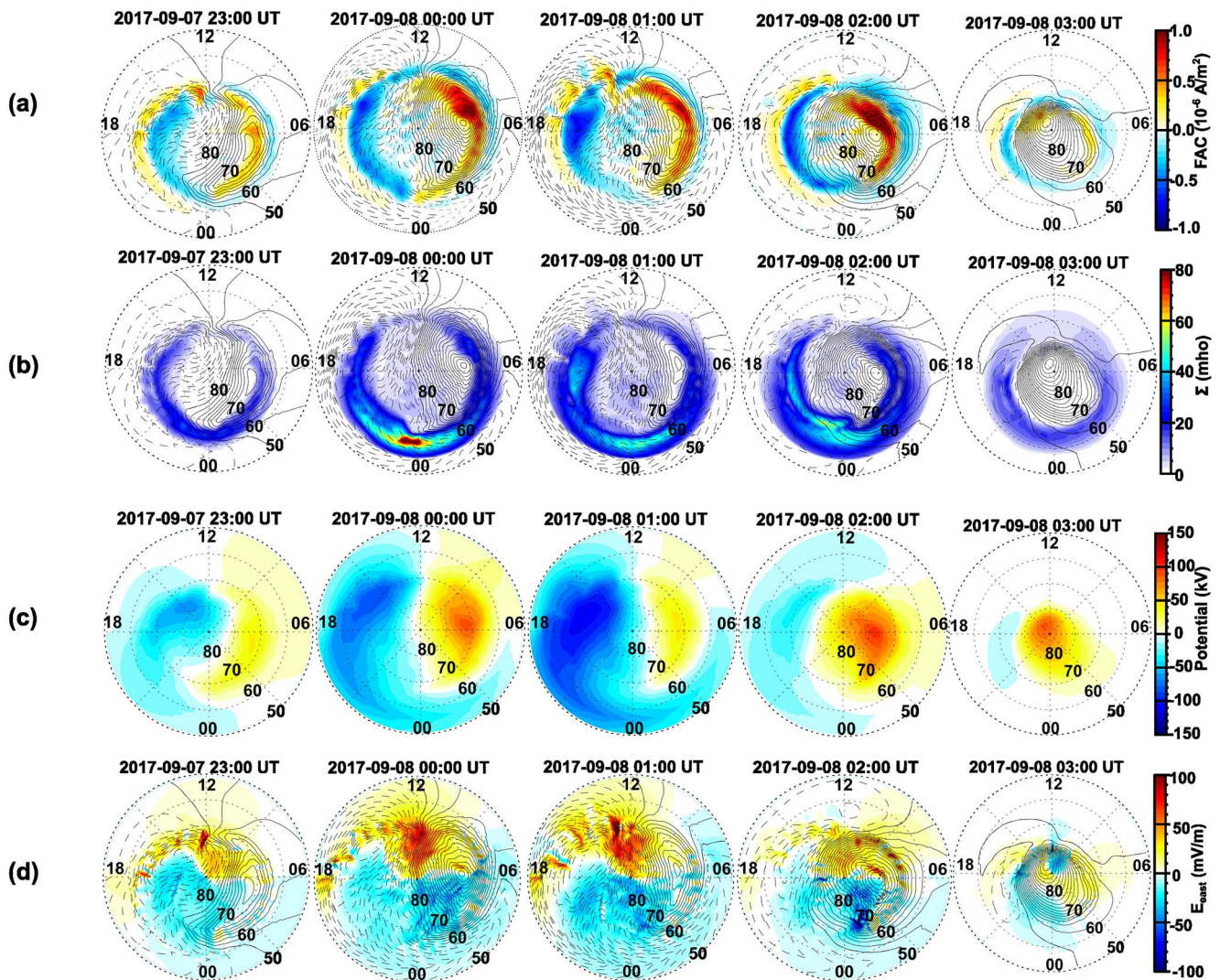


Figure 8. Snapshots of (a) field-aligned current at the ionosphere altitude (positive downward), (b) ionospheric Hall conductivity, (c) the electric potential down to the equator (red for positive and blue for negative potentials), (d) eastward component of the ionospheric electric field in the magnetic latitude and magnetic local time coordinates. The Sun is to the top. In the panels (a), (b) and (d), the contour lines indicate the electric potential (positive dashed line and negative solid line).

Lotko et al., 1987; Siscoe et al., 1991; Siscoe & Sanchez, 1987; Sonnerup, 1980). To determine the exact location for the generation of Region-1 FACs, Ebihara and Tanaka (2022) back-traced the “packets” carrying the perturbation associated with FACs (group velocity of the Alfvén waves) in the reference frame of plasma from the ionosphere. They found that the Region 1 FACs are likely to be generated in the low-latitude magnetopause where the southward component of the IMF leads to the reconnection process. During the process, the newly reconnected magnetic field lines are dragged against the magnetic tension force in the anti-sunward and anti-equatorward directions by the solar wind originated plasma. This leads to the formation of Region-1 FACs. As the FACs arrive at the polar ionosphere, the FACs give rise to twin vortex pattern of the ionospheric convection (electric potential pattern, or the DP2 current) to the satisfaction of the current continuity equation. When one views the ionosphere from space in the Northern Hemisphere, the downward (upward) FACs is connected with divergent (convergent) electric field, namely, divergent (convergent) Pederson current. The associated electric field is primarily in the dawn-to-dusk direction. The Hall current also appears simultaneously

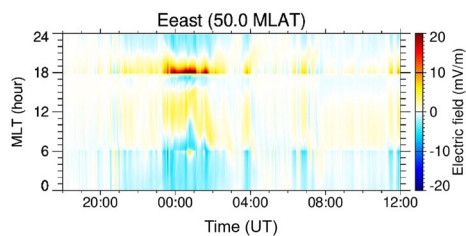


Figure 9. Azimuthal component of the ionospheric electric field (positive eastward) at 50 magnetic latitude (MLAT) as a function of magnetic local time (MLT) and time ranging from 1800 UT on 7 September to 1200 UT on 8 September.

in the clockwise (counterclockwise) direction. The electric fields generated at the high latitude ionosphere penetrates into the lower latitudes and comes down to the to the equatorial region in the inner magnetosphere (Kikuchi, 2005). Non-uniform ionospheric conductivity leads to a modification of the electric potential pattern near the terminator because of the polarization arising from the conductivity gradient (Wolf, 1970). For the DP2 current, which is clockwise on the dawnside and counterclockwise on the duskside, the current is minimal at the equatorward edge of the nightside auroral oval where the ionospheric conductivity is high. Negative space charge is deposited, giving rise to a skew in the convection pattern. This skew is considered as the source of the Harang discontinuity (Tanaka, 2007). When the negative space charge accumulated at the equatorward edge of the nightside auroral oval increases, the skew becomes more significant. Consequently, the region where the westward electric field exits is shifted to the dawnside. This is consistent with the observation of the electric field by (Lejosne & Mozer, 2020) in which the electric field is presumed to be transmitted to the magnetosphere along the magnetic field line (FAC). The westward electric field results in the earthward motion of electrons trapped in the inner magnetosphere due to the EXB drift. After the earthward drift, the electrons undergo the gradient-B and curvature drifts with drift speed depending on the kinetic energy. An observer detects electrons with particular kinetic energies.

Wang et al. (2017) performed test particle simulation with a uniform, constant dawn-to-dusk convection electric field, in which the westward electric field is maximized at midnight, and symmetric with respect to midnight. The zebra stripes of electrons and ions are demonstrated in their simulation. This implies that the presence of the westward electric field is the necessary condition for the formation of the zebra stripes. The influence of the large-scale electric fields have been also recognized at the outer planets like Saturn and Jupiter. Hao et al. (2020) performed a test-particle simulation and compared with the observed zebra stripes to demonstrate that the global-scale noon to midnight electric fields observed at the Saturn and Jupiter can provide a significant adiabatic electron acceleration. Also, Sun et al. (2021) made a statistical analysis of the electron zebra stripes observed between $L = 5-9$ in the Saturnian magnetosphere to suggest that the peak in the zebra stripes are formed from the dayside magnetosphere with a preferred occurrence at 15–18 LT, corresponding to an electric field directed from postnoon to postmidnight. Similarly, the ion spectrograms (30 keV–~1 MeV) recorded by the Cassini spacecraft in the Saturn's inner magnetosphere indicates the importance of noon-midnight electric field for the formation of the ion zebra stripes (Sun et al., 2022).

The zebra stripes are similar to the multiple “nose” structures of keV ions often observed near the inner edge of the plasma sheet (Fennell et al., 1998). Ebihara et al. (2004) performed test particle simulations, and succeeded to reconstruct the spectrograms. They interpreted the multiple “nose” structures in terms of drift echoes of ions, and suggested that the peak fluxes take place at energy given as a function of the drift frequency and the elapsed time. The spectral shape depends largely on the electric field model assumed. Use of realistic electric field model is shown to reconstruct the spectrograms more completely than use of a simple electric field model Ebihara et al. (2004). In our simulation, we employed the electric field obtained by the global MHD simulation with realistic solar wind conditions, and take into account the polarization in the ionosphere. The polarization is one of the possible mechanisms for the skew of the westward electric field as observed by Lejosne and Mozer (2020). However, the simulated spectrograms do not perfectly match the observed ones. The inner edges of the observed zebra stripes are located at $L \sim 1.5$, whereas those obtained by the simulation are located at $L \sim 1.9$. That is, the penetration distance is shorter in the simulation than in the observation. Note that we obtained the magnetospheric electric field by mapping the ionospheric electric field along the magnetic field lines. The ionospheric potential was calculated on the basis of the FACs flowing into and away from the polar ionosphere as described in Section 2.3. The difference in the penetration distance can be explained by relatively small westward electric field in comparison with the actual one. One possibility for the small electric field is that the magnitude of the FACs is smaller than actual. Another possibility is that the ionospheric conductivity is larger than actual. Hence the transmission of these electric fields from the ionosphere to the inner magnetosphere is not sufficient. This results into the difference in the simulated zebra stripes and observed zebra stripes. The electric field is primarily determined by the Region 1 FACs and the ionospheric conductivity. We will investigate these parameters by comparing with observations in future. Apart from this, we think that the electric field variations are qualitatively consistent with the observations. In the simulation, the electric field is largely intensified ~2300 UT on 7 September 2017 as shown in Figure 9. A sharp jump in the observed E_y component ~2300 UT on 7 September 2017 as shown in Figure 2f. The intensification of the electric field could have took place widely as shown in Figure 8c, and played an important role in the redistribution of the electron fluxes and the formation of distinct electron zebra stripes.

Lejosne and Mozer (2020) used data from the Van Allen Probes satellite, and showed that the zebra stripes are usually observed in the presence of prompt penetration electric fields during the substorm onset. It seems that the substorm-associated electric field may be insufficient for the formation of the zebra stripes because the substorm-associated electric field is rather impulsive, and short in the inner magnetosphere as shown by observations (e.g., Dai et al., 2015) and global MHD simulations (Ebihara & Tanaka, 2013). As shown in Figure 6a, it takes about 1–2 hr to accomplish the earthward transport of the electrons that constitute the zebra stripes. Substantial westward electric field lasting for, at least, 1–2 hr would be necessary.

6. Conclusion

The RBSPICE instrument on-board the Van Allen Probe-A spacecraft detected electron zebra stripes during the magnetic storm on 7–8 September 2017. We performed a physics-based simulation for the first time that covers the solar wind-inner magnetosphere coupling processes entirely. The global MHD simulation is used to obtain the electric field in the inner magnetosphere. The electric field is used by the advection simulation that solves the evolution of the phase space density of trapped electrons. Zebra stripes are shown to develop in the simulation. The conclusions are summarized as follows:

- The zebra stripes are essentially the result of drift echoes of the particles that primarily undergo the gradient-B and curvature drifts.
- The electrons comprising the hills of the zebra stripes come from the outer region where the phase space density of the electrons are high.
- The electrons comprising the hills in the zebra stripes preferentially move inward in the pre-midnight to the dusk sector where the westward electric field is significantly enhanced.
- The westward electric field is well elongated to the dawnside. The polarization arising from the gradient of the ionospheric conductivity makes the distribution skew to dawnside. The simulated distribution of the azimuthal component of the electric field is consistent with the observation.

In the future we will compare the simulated electric field and the FACs with the observed ones, and the processes leading to the disappearance of the zebra stripes that were observed during the main phase of the magnetic storm.

Data Availability Statement

The RBSPICE data used in this study are available from (<http://rbspice.ftccs.com/Data.html>). The solar wind data is available at NASA Goddard Space Flight Center's Space Physics Data Facility's OMNIWeb (<https://omniweb.gsfc.nasa.gov/>) service.

Acknowledgments

This study was supported by JSPS KAKENHI Grant 20H01960 and Mission Research at the Research Institute for Sustainable Humanosphere (RISH), Kyoto University. The computer simulation was performed on the KDK computer system at the Research Institute for Sustainable Humanosphere (RISH), Kyoto University. The authors specially thank D. L. Turner for his valuable comments at the VERSIM 2022 meeting.

References

- Birn, J., Thomsen, M. F., Borovsky, J. E., Reeves, G. D., McComas, D. J., & Belian, R. D. (1997). Characteristic plasma properties during dispersionless substorm injections at geosynchronous orbit. *Journal of Geophysical Research*, *102*(A2), 2309–2324. <https://doi.org/10.1029/96ja02870>
- Breneman, A. W., Wygant, J. R., Tian, S., Cattell, C. A., Thaller, S. A., Goetz, K., et al. (2022). The Van Allen probes electric field and waves instrument: Science results, measurements, and access to data. *Space Science Reviews*, *218*(8), 69. <https://doi.org/10.1007/s11214-022-00934-y>
- Bythrow, P. F., Heelis, R. A., Hanson, W. B., Power, R. A., & Hoffman, R. A. (1981). Observational evidence for a boundary layer source of dayside region 1 field-aligned currents. *Journal of Geophysical Research*, *86*(A7), 5577. <https://doi.org/10.1029/ja086a07p05577>
- Christon, S. P., Williams, D. J., Mitchell, D. G., Huang, C. Y., & Frank, L. A. (1991). Spectral characteristics of plasma sheet ion and electron populations during disturbed geomagnetic conditions. *Journal of Geophysical Research*, *96*(A1), 1–22. <https://doi.org/10.1029/90ja01633>
- Cladis, J. B. (1966). Resonance acceleration of particles in the inner radiation belt. In *Radiation trapped in the Earth's magnetic field* (pp. 112–115). Springer. https://doi.org/10.1007/978-94-010-3553-8_9
- Cowley, S. W. H. (1982). The causes of convection in the Earth's magnetosphere: A review of developments during the IMS. *Reviews of Geophysics*, *20*(3), 531. <https://doi.org/10.1029/rg020i003p00531>
- Dai, L., Wang, C., Duan, S., He, Z., Wygant, J. R., Cattell, C. A., et al. (2015). Near-Earth injection of MeV electrons associated with intense dipolarization electric fields: Van Allen Probes observations. *Geophysical Research Letters*, *42*(15), 6170–6179. <https://doi.org/10.1002/2015GL064955>
- Datlowe, D. W., Imhof, W. L., Gaines, E. E., & Voss, H. D. (1985). Multiple peaks in the spectrum of inner belt electrons. *Journal of Geophysical Research*, *90*(A9), 8333. <https://doi.org/10.1029/ja090ia09p08333>
- De Keyser, J., & Echim, M. (2013). Electric potential differences across auroral generator interfaces. *Annales Geophysicae*, *31*(2), 251–261. <https://doi.org/10.5194/angeo-31-251-2013>
- Eastman, T. E., Hones, E. W., Bame, S. J., & Asbridge, J. R. (1976). The magnetospheric boundary layer: Site of plasma, momentum and energy transfer from the magnetosheath into the magnetosphere. *Geophysical Research Letters*, *3*(11), 685–688. <https://doi.org/10.1029/gl003i011p00685>

- Ebihara, Y., Ejiri, M., Nilsson, H., Sandahl, I., Grande, M., Fennell, J. F., et al. (2004). Multiple discrete-energy ion features in the inner magnetosphere: 9 February 1998, event. *Annales Geophysicae*, 22(4), 1297–1304. <https://doi.org/10.5194/angeo-22-1297-2004>
- Ebihara, Y., & Tanaka, T. (2013). Fundamental properties of substorm time energetic electrons in the inner magnetosphere. *Journal of Geophysical Research: Space Physics*, 118(4), 1589–1603. <https://doi.org/10.1002/jgra.50115>
- Ebihara, Y., & Tanaka, T. (2022). Where is region 1 field-aligned current generated? *Journal of Geophysical Research: Space Physics*, 127(3), e2021JA029991. <https://doi.org/10.1029/2021ja029991>
- Ebihara, Y., Tanaka, T., & Kikuchi, T. (2014). Counter equatorial electrojet and overshielding after substorm onset: Global MHD simulation study. *Journal of Geophysical Research: Space Physics*, 119(9), 7281–7296. <https://doi.org/10.1002/2014ja020065>
- Echim, M. M., Roth, M., & De Keyser, J. (2008). Ionospheric feedback effects on the quasi-stationary coupling between LLBL and postnoon/evening discrete auroral arcs. *Annales Geophysicae*, 26(4), 913–928. <https://doi.org/10.5194/angeo-26-913-2008>
- Fennell, J. F., Chen, M. W., Roeder, J. L., Peterson, W. K., & Trattner, K. J. (1998). Multiple discrete-energy ion features in the inner magnetosphere: Polar observations. *Physics of Plasmas*, 14.
- Hao, Y.-X., Sun, Y.-X., Roussos, E., Liu, Y., Kollmann, P., Yuan, C.-J., et al. (2020). The formation of Saturn's and Jupiter's electron radiation belts by magnetospheric electric fields. *The Astrophysical Journal*, 905(1), L10. <https://doi.org/10.3847/2041-8213/abc3f>
- Iijima, T. (2000). Field-aligned currents in geospace: Substance and significance. In *Magnetospheric current systems* (pp. 107–129). American Geophysical Union. <https://doi.org/10.1029/gm118p0107>
- Imhof, W. L., Gaines, E. E., & Reagan, J. B. (1973). Dynamic variations in intensity and energy spectra of electrons in the inner radiation belt. *Journal of Geophysical Research*, 78(22), 4568–4577. <https://doi.org/10.1029/ja078i022p04568>
- Imhof, W. L., Gaines, E. E., & Reagan, J. B. (1981). High-resolution spectral features observed in the inner radiation belt trapped electron population. *Journal of Geophysical Research*, 86(A4), 2341. <https://doi.org/10.1029/ja086ia04p02341>
- Imhof, W. L., & Smith, R. V. (1965). Observation of nearly monoenergetic high-energy electrons in the inner radiation belt. *Physical Review Letters*, 14(22), 885–887. <https://doi.org/10.1103/physrevlett.14.885>
- Imhof, W. L., & Smith, R. V. (1966). Low altitude measurements of trapped electrons. In *Radiation trapped in the Earth's magnetic field* (pp. 100–111). Springer.
- Johnson, J. R., & Wing, S. (2015). The dependence of the strength and thickness of field-aligned currents on solar wind and ionospheric parameters. *Journal of Geophysical Research: Space Physics*, 120(5), 3987–4008. <https://doi.org/10.1002/2014ja020312>
- Jordanova, V. K., Thorne, R. M., Li, W., & Miyoshi, Y. (2010). Excitation of whistler mode chorus from global ring current simulations. *Journal of Geophysical Research*, 115(A5), A00F10. <https://doi.org/10.1029/2009ja014810>
- Kikuchi, T. (2005). Transmission line model for driving plasma convection in the inner magnetosphere. *The Inner Magnetosphere: Physics and Modeling*, 155, 173–179. <https://doi.org/10.1029/155gm20>
- Kikuchi, T., Lühr, H., Kitamura, T., Saka, O., & Schlegel, K. (1996). Direct penetration of the polar electric field to the equator during DP 2 event as detected by the auroral and equatorial magnetometer chains and the EISCAT radar. *Journal of Geophysical Research*, 101(A8), 17161–17173. <https://doi.org/10.1029/96ja01299>
- King, J. H., & Papitashvili, N. E. (2005). Solar wind spatial scales in and comparisons of hourly Wind and ACE plasma and magnetic field data. *Journal of Geophysical Research*, 110(A2), 1–9. <https://doi.org/10.1029/2004JA010649>
- King, J. H., & Papitashvili, N. E. (2020). OMNI 1-min data set. NASA Space Physics Data Facility. <https://doi.org/10.48322/45BB-8792>
- Lax, P., & Wendroff, B. (1960). Systems of conservation laws. *Communications on Pure and Applied Mathematics*, 13(2), 217–237. <https://doi.org/10.1002/cpa.3160130205>
- Lejosne, S., Fejer, B. G., Maruyama, N., & Scherliess, L. (2022). Radial transport of energetic electrons as determined from the zebra stripes measured in the Earth's inner belt and slot region. *Frontiers in Astronomy and Space Sciences*, 9, 823695. <https://doi.org/10.3389/fspas.2022.823695>
- Lejosne, S., & Mozer, F. S. (2020). Experimental determination of the conditions associated with zebra stripe pattern generation in the Earth's inner radiation belt and slot region. *Journal of Geophysical Research: Space Physics*, 125(7), e2020JA027889. <https://doi.org/10.1029/2020ja027889>
- Lejosne, S., & Roederer, J. G. (2016). The “zebra stripes”: An effect of F region zonal plasma drifts on the longitudinal distribution of radiation belt particles. *Journal of Geophysical Research: Space Physics*, 121(1), 507–518. <https://doi.org/10.1002/2015ja021925>
- Liu, Y., Zong, Q., Zhou, X., Foster, J. C., & Rankin, R. (2016). Structure and evolution of electron zebra stripes in the inner radiation belt. *Journal of Geophysical Research: Space Physics*, 121(5), 4145–4157. <https://doi.org/10.1002/2015ja022077>
- Lotko, W., Sonnerup, B. U. Ö., & Lysak, R. L. (1987). Nonsteady boundary layer flow including ionospheric drag and parallel electric fields. *Journal of Geophysical Research*, 92(A8), 8635. <https://doi.org/10.1029/ja092ia08p08635>
- Mauk, B. H., Fox, N. J., Kanekal, S. G., Kessel, R. L., Sibeck, D. G., & Ukhorskiy, A. (2012). Science objectives and rationale for the radiation belt storm probes mission. *Space Science Reviews*, 179(1–4), 3–27. <https://doi.org/10.1007/s11214-012-9908-y>
- Mitchell, D. G., Lanzerotti, L. J., Kim, C. K., Stokes, M., Ho, G., Cooper, S., et al. (2013). Radiation belt storm probes ion composition experiment (RBSPICE). *Space Science Reviews*, 179(1–4), 263–308. <https://doi.org/10.1007/s11214-013-9965-x>
- Nishida, A. (1968). Coherence of geomagnetic DP 2 fluctuations with interplanetary magnetic variations. *Journal of Geophysical Research*, 73(17), 5549–5559. <https://doi.org/10.1029/ja073i017p05549>
- Northrop, T. G. (1963). Adiabatic charged-particle motion. *Reviews of Geophysics*, 1(3), 283. <https://doi.org/10.1029/rg001i003p00283>
- Roe, P. L. (1985). Some contributions to the modelling of discontinuous flows. In *Large-Scale Computations in Fluid Mechanics* (pp. 163–193). Springer.
- Roederer, J. G. (1970). *Dynamics of geomagnetically trapped radiation*. Springer Berlin Heidelberg. <https://doi.org/10.1007/978-3-642-49300-3>
- Sauvaud, J.-A., Walt, M., Delcourt, D., Benoist, C., Penou, E., Chen, Y., & Russell, C. T. (2013). Inner radiation belt particle acceleration and energy structuring by drift resonance with ULF waves during geomagnetic storms. *Journal of Geophysical Research: Space Physics*, 118(4), 1723–1736. <https://doi.org/10.1002/jgra.50125>
- Senior, C., & Blanc, M. (1984). On the control of magnetospheric convection by the spatial distribution of ionospheric conductivities. *Journal of Geophysical Research*, 89(A1), 261–284. <https://doi.org/10.1029/JA089iA01p00261>
- Siscoe, G. L., Lotko, W., & Sonnerup, B. U. Ö. (1991). A high-latitude, low-latitude boundary layer model of the convection current system. *Journal of Geophysical Research*, 96(A3), 3487. <https://doi.org/10.1029/90ja02362>
- Siscoe, G. L., & Sanchez, E. (1987). An MHD model for the complete open magnetotail boundary. *Journal of Geophysical Research*, 92(A7), 7405. <https://doi.org/10.1029/ja092ia07p07405>
- Sonnerup, B. U. (1980). Theory of the low-latitude boundary layer. *Journal of Geophysical Research*, 85(A5), 2017. <https://doi.org/10.1029/ja085ia05p02017>
- Sun, Y. X., Hao, Y. X., Roussos, E., Zong, Q. G., Liu, Y., Zhou, X. Z., et al. (2022). Zebra stripe patterns in energetic ion spectra at Saturn. *Geophysical Research Letters*, 49(4), e2021GL097691. <https://doi.org/10.1029/2021GL097691>

- Sun, Y. X., Roussos, E., Hao, Y. X., Zong, Q. G., Liu, Y., Lejosne, S., et al. (2021). Saturn's inner magnetospheric convection in the view of zebra stripe patterns in energetic electron spectra. *Journal of Geophysical Research: Space Physics*, *126*(10), 1–13. <https://doi.org/10.1029/2021JA029600>
- Tanaka, T. (1994). Finite volume TVD scheme on an unstructured grid system for three dimensional MHD simulation of inhomogeneous systems including strong background magnetic fields. *Journal of Computational Physics*, *111*(2), 381–389. <https://doi.org/10.1006/jcph.1994.1071>
- Tanaka, T. (2007). Magnetosphere ionosphere convection as a compound system. *Space Science Reviews*, *133*(1–4), 1–72. <https://doi.org/10.1007/s11214-007-9168-4>
- Tanaka, T. (2015). *Substorm auroral dynamics reproduced by advanced global magnetosphere-ionosphere (MI) coupling simulation* (pp. 177–190). Wiley. <https://doi.org/10.1002/9781118978719.ch13>
- Tsunomura, S. (1999). Numerical analysis of global ionospheric current system including the effect of equatorial enhancement. *Annales Geophysicae*, *17*(5), 692–706. <https://doi.org/10.1007/s00585-999-0692-2>
- Turner, D. L., O'Brien, T. P., Fennell, J. F., Claudepierre, S. G., Blake, J. B., Jaynes, A. N., et al. (2017). Investigating the source of near-relativistic and relativistic electrons in Earth's inner radiation belt. *Journal of Geophysical Research: Space Physics*, *122*(1), 695–710. <https://doi.org/10.1002/2016JA023600>
- Ukhorskiy, A. Y., Sitnov, M. I., Mitchell, D. G., Takahashi, K., Lanzerotti, L. J., & Mauk, B. H. (2014). Rotationally driven 'zebra stripes' in Earth's inner radiation belt. *Nature*, *507*(7492), 338–340. <https://doi.org/10.1038/nature13046>
- Wang, Y., Zong, Q., & Zhou, X. (2017). Test particle simulation on the ion and electron zebra stripes and their time evolution in inner radiation belt. *Science China Technological Sciences*, *61*(4), 623–632. <https://doi.org/10.1007/s11431-016-9087-x>
- Williams, D. J., & Frank, L. A. (1984). Intense low-energy ion populations at low equatorial altitudes. *Journal of Geophysical Research*, *89*(A6), 3903. <https://doi.org/10.1029/ja089ia06p03903>
- Wolf, R. A. (1970). Effects of ionospheric conductivity on convective flow of plasma in the magnetosphere. *Journal of Geophysical Research*, *75*(25), 4677–4698. <https://doi.org/10.1029/ja075i025p04677>
- Wygant, J. R., Bonnell, J. W., Goetz, K., Ergun, R. E., Moer, F. S., Bale, S. D., et al. (2013). The electric field and waves instruments on the radiation belt storm probes mission. *Space Science Reviews*, *179*(1), 183–220. <https://doi.org/10.1007/s11214-013-0013-7>
- Xiao, F., Thorne, R. M., & Summers, D. (1998). Instability of electromagnetic R-mode waves in a relativistic plasma. *Physics of Plasmas*, *5*(7), 2489–2497. <https://doi.org/10.1063/1.872932>